Fast calculation of spatial potentials and robust inversion of field sources for overhead transmission lines in complex terrain

Original
Fast calculation of spatial potentials and robust inversion of field sources for overhead transmission lines in complex terrain / Ji, Yuqing; Yuan, Jiaxin; Stievano, Igor S.; Trinchero, Riccardo; Zhou, Hang. - In: ELECTRIC POWER SYSTEMS RESEARCH. - ISSN 0378-7796. - ELETTRONICO. - 246:(2025), pp. 1-12. [10.1016/j.epsr.2025.111686]

Publisher:
Elsevier

Published
DOI:10.1016/j.epsr.2025.111686

Fast Calculation of Spatial Potentials and Robust Inversion of Field Sources for Overhead Transmission Lines in Complex Terrain

Yuqing Ji [a], Jiaxin Yuan [a,*], Igor S. Stievano [b,*], Riccardo Trinchero [b], Hang Zhou [a]

[a] *State Key Laboratory of Power Grid Environmental Protection, School of Electrical Engineering and Automation, Wuhan University, China*
[b] *Electromagnetic Compatibility Group, Department of Electronics and Telecommunications, Politecnico di Torino, 10129 Torino, Italy*

***Abstract*—To achieve real-time monitoring of spatial potential and field source voltage of overhead lines in complex terrain, this paper proposes a numerical model for fast forward calculation of spatial potential and robust inversion calculation of field source voltage. The main problem addressed is the computational complexity and accuracy issues associated with traditional numerical methods and simplified engineering methods, which often fail to provide real-time and reliable results in complex terrain environments. This study aims to develop a more efficient and accurate numerical model for real-time monitoring. Specifically, a simplified cross-section model based on the constant boundary element method (BEM) and an unstructured discretization method is established. This model allows for faster forward calculations of spatial potential. Additionally, a robust inversion method based on the optimization of the measurement array structure is presented. This method ensures the accuracy and reliability of the inversion of field source voltage. The effectiveness of the proposed method is demonstrated through both 2-D analytical cases and 3-D cases. The forward calculation time is significantly reduced to less than one voltage cycle (50 Hz), which is crucial for real-time monitoring. Furthermore, the inversion uncertainty is less than 3E-3 p.u., and the inversion error is less than 1.5%.**

***Keywords:* Transmission line monitoring; voltage monitoring; noncontact monitoring.**

1. INTRODUCTION

Currently, overhead transmission lines are in complex transmission environments, which are affected by different terrain [1] and vegetation coverage [2]. The numerical model of the electromagnetic environment of transmission lines is an important foundation for human protection [3], equipment design [4], state monitoring [5], and risk assessment [6]. The important applications of state monitoring are forward evaluation of spatial potential distribution and inversion monitoring of transmission line field source information based on spatial electromagnetic information.

Due to the influence of terrain and vegetation, there is no analytical solution for calculating the spatial potential distribution of transmission lines [7], and only numerical or semi-analytical methods can be used. However, general numerical methods have high computational complexity problems [8]. Meanwhile, inversion calculations are affected by the ill-posed characteristics of complex modeling, making it difficult to obtain stable and reliable solutions [9]. Currently, there is no literature report on both solving the problems of forward computational complexity and inversion computational reliability in complex terrain.

Many scholars have conducted relevant research on the forward calculation of spatial potential. 2-D charge simulation method (CSM) was used in [10] to calculate the spatial potential under flat ground conditions for the first time, and this method became a recommended engineering method for CIGRE [11] and IEEE [12] standards. However, this method lacks consideration for actual complex terrain environments and simplifies calculations directly, resulting in significant errors [13]. The researchers in [14] carried out a detailed study on the impact of vegetation such as trees and found that it can be equivalent to terrain calculation. The work in [15] centered around analyzing the impact of towers at different heights of terrain on the magnetic field calculation using integration method under linear terrain conditions. The study in [16] applied Finite Element Method (FEM) to studying slope terrain and found that there was a significant increase in electric field near the ground compared to flat terrain. [17] improved FEM calculation near line conductors using Kelvin transformation methods, saving more than 74% of time compared to traditional FEM. A hybrid FEM method was developed in [18] to calculate the electromagnetic distribution inside the substation using surface impedance method and simplified analytical solution. In [19], the fast multipole method (FMM) - BEM method was proposed to solve the 2-D Laplace potential problem reduces the computational complexity of BEM from $O(N^3)$ to $O(N\log N)$. The method of moments (MoM) was applied in [20] to analyze potential, which is more suitable for semi-infinite domain problems and effectively reduced the number of elements compared to FEM. A fast adaptive BEM was used in [21] to analyze the electric field under complex terrain, the calculation time was shortened from 3 minutes to 2 seconds. [22] proposed an analytical model based on conformal transformation for symmetrical mountain terrain, but only simple symmetrical shapes can be solved. [23] used Fourier transform enhanced CSM to calculate the spatial potential of transmission lines considering flat ground conditions with space charges. Currently, there is limited research on the calculation method of spatial potential for overhead lines in complex terrains, and further exploration is needed. Overall, for complex terrain potential calculation problems in semi-infinite domains, the semi-analytical BEM based on boundary decomposition numerical method is more suitable for general situations, with lower computational complexity than the FEM based on domain decomposition.

Regarding the inversion problem of transmission line sources, it should be clarified that inversion is only possible when the forward calculation is valid. It is worth noting that inverse analysis is primarily used for non-contact monitoring of field sources [24], while most non-contact monitoring studies overlook the impact of complex terrain, leading to significant errors, especially in scenarios that require real-time monitoring [25]. Meanwhile, commonly used inversion calculation methods often encounter the ill-posed characteristics, such as error amplification and instability of solutions. To solve this, many studies have made beneficial attempts. [26] designed spatial matrix operators using regularization methods of unstructured networks to solve inversion problems of complex terrain. [27] adopted a stochastic optimization strategy to solve magnetic field reconstruction. [28] adopted comprehensive method of interior method and metaheuristic algorithm to transform the line parameter reconstruction problem into a nonlinear optimization problem. [29] proposed an enhanced relative phase method by utilizing the spatial phasor characteristics of the field source, which improved the sensitivity of inversion. [30] considered electromagnetic inversion under complex terrain and established a sensitivity matrix using the gauss-newton method. [31] developed an efficient inversion method for nonlinear inversion problems of complex terrain field sources using rational Krylov subspace method. [32] and [33] proposed using iterative methods such as paper swarm optimization (PSO) to solve nonlinear equations and obtain field source information. For complex problems, iterative methods are relatively stable, but they also introduce high computational complexity [34], which remains a challenging problem for real-time monitoring.

This study addresses the challenge of real-time monitoring of spatial potential and field source voltage for overhead lines in complex terrain. According to the above review, traditional methods have high computational complexity or low accuracy, and are difficult to monitor in real-time. To overcome these issues, a numerical model is proposed for fast forward calculation of spatial potential and robust inversion calculation of field source voltage. The input parameters include geometric parameters of the overhead lines, terrain data, and measurement array structures. The output results are the forward calculation of spatial potential and the inversion of field source voltage. If terrain complexity is not considered, traditional methods suffer from significant computational delays and reduced accuracy, making real-time monitoring unreliable. Our approach involves establishing a simplified cross-section model based on the constant BEM and an unstructured discretization method. This model allows for faster and more accurate forward calculations. Additionally, a robust inversion method is also developed based on the optimization of the measurement array structure to ensure accurate and reliable inversion of field source voltage. This study aims to provide a robust and efficient numerical model for real-time monitoring, thereby enhancing the reliability and accuracy of overhead line monitoring systems.

This paper is organized as follows. Section 2 established a detailed model of the terrain and the lines, as well as a simplified 2-D cross-sectional model. Section 3 presented the semi-analytical forward calculation method and unstructured discretization strategy. Section 4 derived the inversion calculation model and established a performance analysis method. Section 5 adopted the verification methods of 2-D analytical examples and 3-D simulation examples and discussed them. Section 6 summarized this paper.

2. METHOD

2.1 The model of transmission lines and terrain

Firstly, according to general engineering design principles, it can be assumed that the three-phase transmission line is a catenary with equal height suspension and uniform load, and an equivalent single conductor is used instead of split conductors. Assuming the electric field is a quasi-steady field, the spatial media is linear and uniform. The measurement array has no significant effect on the field source [11]. A coordinate system based on the center of Phase B on the ground as the origin, as shown in Fig. 1. The math model for transmission lines is shown in (1), where subscript $_P$ represents Phase, θ_P is the plane wind deflection angle of the conductor, D_P is the span length, h_P is the height of the suspension point, and S_P is the maximum sag. λ_P is the stress coefficient of the conductor and can be calculated through S_P.

$$\begin{cases} y = \cos\theta_p \left(\dfrac{D_p}{\lambda_p}\left(\cosh\dfrac{\lambda_p z}{D_p} - \cosh\dfrac{\lambda_p}{2}\right)\right) + h_p \\ x = -\sin\theta_p \left(\dfrac{D_p}{\lambda_p}\left(\cosh\dfrac{\lambda_p z}{D_p} - \cosh\dfrac{\lambda_p}{2}\right)\right) \\ S_p = \dfrac{D_p}{\lambda_p}\left(\cosh\dfrac{\lambda_p}{2} - 1\right) \\ -\dfrac{D_p}{2} \le z \le \dfrac{D_p}{2} \end{cases} \tag{1}$$

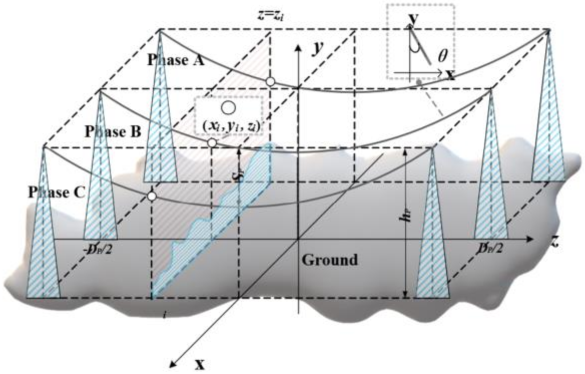

Fig. 1. Model of transmission lines in complex terrain.

Then, assuming that the shielding objects such as the terrain and vegetation are good conductors, the terrain satisfies the relationship as shown in (2), and the range is limited to one span. Due to the presence of grounding towers, solutions at the end are unreliable. The impact of the ground wire is relatively small, so it is ignored.

$$z = f(x, y), \ -\frac{D_p}{2} < z < \frac{D_p}{2} \tag{2}$$

Thus, the problem can be equivalent to a calculation in complex terrain. Meanwhile, we will take a 2-D cross-section as the model to simplify. When the measurement point is located on the $z=z_i$ plane, select the intersection point of the cross-section and the conductor at that location, and assume that the source conductor at the cross-section is infinitely long and parallel to the ground. Establish a simplified calculation model as shown in (3). Since z is known at this point, the relationship between the terrain x and y coordinates can be obtained from (2). It can be written as f_1, where L_m is the solution range. A typical value of L_m can be taken as $5h_P$. For measurement points in the near zone, the contribution of distant region components greater than L_m to the integral equation is relatively small. The simplified model diagram is shown in Fig. 2.

$$y = f_1(x), \ -L_m \le x \le L_m \tag{3}$$

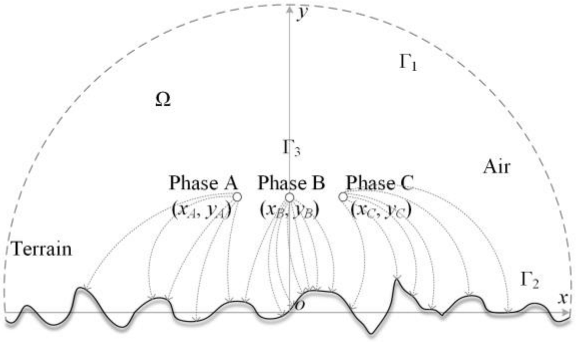

Fig. 2. Schematic diagram of 2-D simplified solution.

Let the solution region be Ω, which includes transmission lines, terrain, and a semi-infinite solution domain, and is enclosed by its boundary Γ; Let the semi-infinite boundary be Γ_1, the uneven terrain be Γ_2, the wire boundary be Γ_3, and the boundary satisfy (4).

$$\begin{gathered} \Gamma = \Gamma_1 \cup \Gamma_2 \cup \Gamma_3 \\ \Gamma_1 \cap \Gamma_3 = \varnothing, \ \Gamma_2 \cap \Gamma_3 = \varnothing \end{gathered} \tag{4}$$

This problem satisfies the 2-D Laplace equation and boundary conditions is as (5). Among them, (x, y) represents the points within the domain, φ represents the potential and φ_n represents the normal derivative of potential. The potential of the terrain is 0 and superscripts represent the given boundary values.

$$\begin{cases} \nabla^2 \varphi(x, y) = 0 \ \ \forall \mathrm{x}, \mathrm{y} \in \Omega \\ \varphi_n(x, y) = 0 \ \ \forall \mathrm{x}, \mathrm{y} \in \Gamma_1 \\ \varphi(x, y) = 0 \ \ \forall \mathrm{x}, \mathrm{y} \in \ \Gamma_2 \\ \varphi(x, y) = \overline{\varphi_3}(x, y) \ \ \forall \mathrm{x}, \mathrm{y} \in \Gamma_3 \end{cases} \tag{5}$$

2.2 *Constant BEM*

After establishing the model, the constant BEM was used for analysis. p_1 is the collocation point within the domain Ω, and p_2 is the field point on the Γ. The boundary value problem described in (5) can be transformed into a boundary integral equation (BIE). H replaces the normal derivative of the Green's function G. Then, discretize the boundary Γ into N constant elements and number them, with the midpoint of each element as the node. The known boundary conditions are set as constant at each point on the element and equal to the boundary values of the element node. The enlarged schematic diagram of the discretized model and elements is shown in Fig. 3.

Below is the discretized BIE, which is integrated into a sum form as (6). For points p_i and p_j on the boundary Γ, their potentials are φ_i and φ_j, and the corresponding $G(p_i, p_j)$ and $H(p_i, p_j)$ are also written as G_{ij} and H_{ij}. The normal derivative of the potential is abbreviated as φ_{nj}.

$$\frac{1}{2}\varphi_i = -\sum_{j=1}^{N}\left[G_{ij}\varphi_{nj} - H_{ij}\varphi_j\right] \qquad (6)$$

$$for\ i = 1,\ 2,\ \cdots,\ N.\ j = 1,\ 2,\ \cdots,\ N.$$

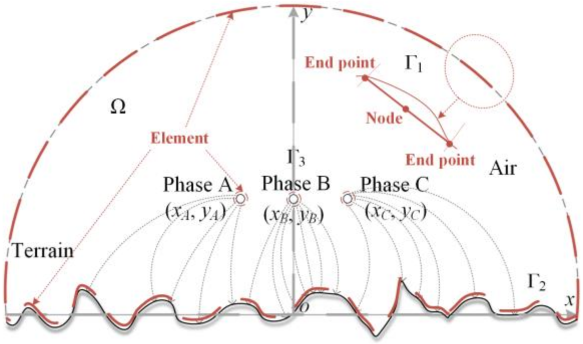

Fig. 3. Discretization of the model.

When observing (5) and (6), it can be seen that the discrete nodes on the semi-infinite boundary Γ_1 are far away from the field source point, and the potential amplitude on Γ_1 can be approximately calculated by the image method to be small. When calculating the potential of measurement points near the field source, the contribution of Γ_1 in (6) can be further ignored. The rest part only has Dirichlet boundary conditions, all terms involving G_{ij} are unknown. Based on this, (6) can be further transformed into matrix form as (7) and similar terms can be merged. [] and $[G]$ are both $N*N$ square matrices, while $[\varphi_{\boldsymbol{n}}]$ and $[\varphi]$ are $N*1$ vectors. Obviously, the left side of the equation is the unknown term, and the left side of the equation is known. The system of linear equations $[A][x]=[b]$ has the same form and can be solved using similar methods. Among them, $[A]$ is $[G]$, $[x]$ is $[\varphi_{\boldsymbol{n}}]$, and $[b]$ is $[][\varphi]$.

$$\begin{gathered}[G][\varphi_{\boldsymbol{n}}] = [\hat{H}][\varphi] \\ \hat{H}_{ij} = H_{ij} - \frac{1}{2}\delta_{ij},\ \delta_{ij} = \begin{cases} 1,\ i = j \\ 0,\ i \neq j \end{cases}\end{gathered} \qquad (7)$$

Solving for (7) yields $[\varphi_{\boldsymbol{n}}]$, which can be substituted into the BIE of the measurement point p_m to calculate the potential of unknown points within the domain (non-boundary). It can also be written in the form of (8), where the subscript $_m$ represents the measurement value and its corresponding coupling matrix. The relationship between the unknown phase lines voltage and the equations requires m to be at least three. In this paper, the research object is a single-circuit lines, and m can be taken as three to establish the equation. (8) can also be extended to the case of multi-circuit lines.

$$[\varphi_m] = [H_m][\varphi] - [G_{\mathrm{m}}][\varphi_{\boldsymbol{n}}] \qquad (8)$$

Thus, the 2-D Laplace equation under Dirichlet conditions is solved using the constant BEM, and a semi-analytical solution for the potential is provided for subsequent computer solutions. It is worth noting that this problem can be viewed as an outer boundary containing three non-intersecting hole boundaries. The multiple-connected domain can be transformed into a simply connected domain, for the electrostatic field is irrotational and independent of the choice of integration path.

2.3 *Unstructured discretization*

When directly solving for (7) and (8), the computational complexity is $O(N^3)$. When using equal interval discretization without processing, to simultaneously meet the calculation accuracy of different sized objects, the discretization interval must be relatively small, and the terrain solution radius L_m must be at least the width of the transmission corridor. The estimation of general transmission line parameters and terrain parameters shows that equidistant discretization will easily result in large number of units N, as shown in Fig. 4 (a).

The spatial potential predominantly weakens with increasing distance. Therefore, the highly sensitive area of the measurement points is smaller than the entire solution area. Therefore, based on this conclusion, we can use unstructured discretization ideas to accelerate the solving process, that is, using refined grids in the local "near-zone" where the measurement point is located, and using rougher grids in the "far-zone" farther away from the measurement point. This is different from adaptive discretization, where unstructured discretization is built around measurement points, while adaptive discretization is implemented around the structure of the field source model.

For the specific problem of solving the spatial potential of transmission lines in complex terrain, unstructured discretization is further optimized. Since the size of the lines is much smaller than that of the terrain, placing measurement points near the conductor lines can effectively reduce the number of discretization elements of the terrain. At the same time, due to the small size of the lines, there is no need for overly refined grids. The influence of line conductors on the ground electric field is mainly concentrated in the width of the transmission corridor, so the subdivision of the ground can be gradually refined from the corridor radius according to the distance. It can also be divided into three levels of subdivision: first level lines, second level transmission corridor and third level the external shape.

This specific unstructured discretization approach can lead to the following discretization steps, as shown in Fig. 4 (b):

Step 1: Establish a progressively decreasing global grid based on the basic size relationship between the lines and terrain.

Step 2: Extract the corresponding elements from the global grid of *Step 1* based on the distance range of the measurement points.

Step 3: Expand the grid outward and reconstruct the local grid with the elements of *Step 2* as the core.

Step 4: Arrange progressively refined discrete points on the outer boundary of the local discretization to ensure the smoothness of the discretization.

Step 5: Due to the consistency in the local and global grids, the information computed locally can be accurately mapped to the global grid.

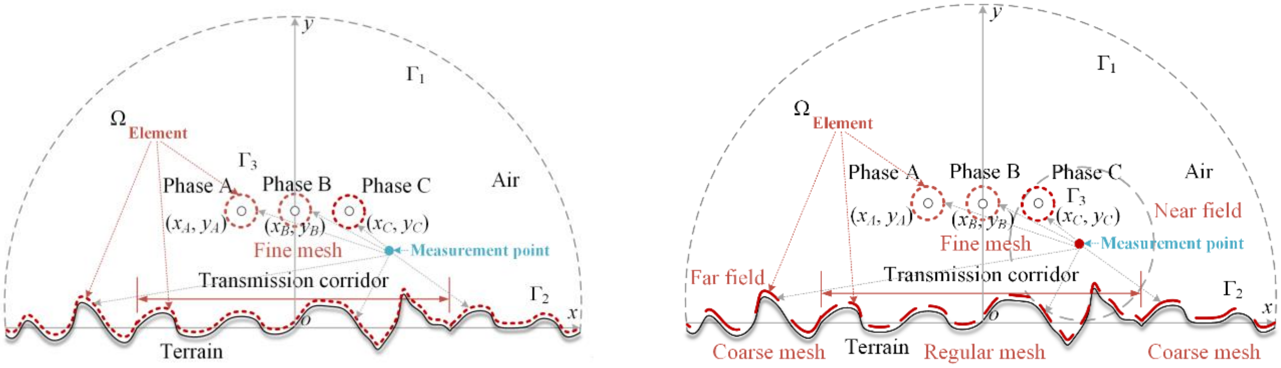

(a) (b)

Fig. 4. Comparison before and after optimization of discretization (a) equally spaced discretization (b) unstructured discretization.

The time complexity of directly solving the boundary element method is $O(N^3)$, therefore, due to the simplification of unstructured discretization, the number of solving elements N is greatly reduced. Further reduce the complexity of the solution and achieve the goal of fast solving.

2.4 Inverse analysis

After establishing a forward solving model, this paper continues to study robust inversion. Due to the natural characteristics of the BEM, there is little difference in geometric features between each element, especially in adjacent elements, which leads to coefficient closeness in the generated linear equation system, directly resulting in the ill-posed characteristics of the coefficient matrix [*A*]. Even small measurement errors can be amplified by the ill-conditioned coefficient matrix, resulting in unacceptable results. The core of inversion calculation research is how to achieve stable and reliable reconstruction of field source values based on measurement data contaminated by noise.

$$
\begin{aligned}
&[G]=\begin{bmatrix} G_{tt} & G_{tl} \\ G_{lt} & G_{ll} \end{bmatrix},\ [\hat{H}]=\begin{bmatrix} \hat{H}_{tt} & \hat{H}_{tl} \\ \hat{H}_{lt} & \hat{H}_{ll} \end{bmatrix}, \\
&[\varphi]=\begin{bmatrix} \varphi_{t} \\ \varphi_{l} \end{bmatrix},\ [\varphi_{n}]=\begin{bmatrix} \varphi_{nt} \\ \varphi_{nl} \end{bmatrix},\ [\varphi_{t}]=\mathbf{0} \\
&\xrightarrow{(7)} \begin{bmatrix} G_{tt} & G_{tl} \\ G_{lt} & G_{ll} \end{bmatrix}\begin{bmatrix} \varphi_{nt} \\ \varphi_{nl} \end{bmatrix}=\begin{bmatrix} \hat{H}_{tl} \\ \hat{H}_{ll} \end{bmatrix}[\varphi_{l}] \\
&\xrightarrow{inverse} \begin{bmatrix} \varphi_{nt} \\ \varphi_{nl} \end{bmatrix}=\left[G\right]^{-1}\begin{bmatrix} \hat{H}_{tl} \\ \hat{H}_{ll} \end{bmatrix}[\varphi_{l}] \\
&\xrightarrow{(8)} [\varphi_{m}]=\left(\begin{bmatrix} H_{mt} & H_{ml} \end{bmatrix}\begin{bmatrix} \varphi_{t} \\ \varphi_{l} \end{bmatrix}-\begin{bmatrix} G_{mt} & G_{ml} \end{bmatrix}\begin{bmatrix} \varphi_{nt} \\ \varphi_{nl} \end{bmatrix}\right) \\
&\xrightarrow{[\varphi_{t}]=\mathbf{0}} [\varphi_{m}]=\left(H_{ml}-\begin{bmatrix} G_{mt} & G_{ml} \end{bmatrix}[G]^{-1}\begin{bmatrix} \hat{H}_{tl} \\ \hat{H}_{ll} \end{bmatrix}\right)[\varphi_{l}] \\
&\xrightarrow{inverse} [\varphi_{l}]=\left(H_{ml}-\begin{bmatrix} G_{mt} & G_{ml} \end{bmatrix}[G]^{-1}\begin{bmatrix} \hat{H}_{tl} \\ \hat{H}_{ll} \end{bmatrix}\right)^{-1}[\varphi_{m}] \\
&\xrightarrow{simplify} [\varphi_{l}]=[F]^{-1}[\varphi_{m}]
\end{aligned}
\tag{9}
$$

Firstly, assuming that the field source voltage is unknown, based on the boundary solution calculation (7) and the measurement point value calculation (8) in the forward solution model, the following inversion model (9) can be derived. Specifically, the relationship between the field source potential $[\varphi_l]$ and the boundary normal derivative of the potential $[\varphi_{\boldsymbol{n}}]$ is established by (7), and the above relationship is substituted into (8) to establish the inversion between the measurement point potential $[\varphi_m]$ and the field source potential $[\varphi_l]$ as (9). Firstly, the matrix form equation for calculating the spatial potential under irregular terrain is first established by (7). Then, the matrix corresponding to the Green's function in (7) is inverted and substituted into the coupling matrix (8) for calculating the measurement point values. At the same time, the boundary condition with ground point values set to 0 is applied to simplify the above expression. Inverting again leads to the expression of the field source voltage in terms of the measurement point values as (9), and the coefficient matrix is denoted as [F]. Among them, the subscript $_t$ represents terrain, and the subscript $_l$ represents line. The last equation in (9) provides the inversion matrix relationship between the measuring point values and the field source potential values. Like (8), since the unknown is three-phase voltage, corresponding to a minimum of 3 measurement points. The inversion coefficient matrix $[F]$ is a 3*3 matrix. When solving multi-circuit transmission lines problems, (9) can be simply extended.

Observing (9), the properties of the inversion coefficient matrix $[F]$ are composed of multiple coefficient matrices with complex components, making it difficult to directly derive its behavior characteristics through derivation. According to the general formula of the condition number [35], (9) satisfies the inequality relationship as (10), where Δ represents the change value, * represents the true value, and κ represents the condition number. From (10), the coefficient matrix error is not large, the calculation error of the field source value is determined by the measurement error amplified by the condition number of the coefficient matrix. The key to obtaining stable and accurate solutions is to reduce the condition number of the inversion coefficient matrix.

$$
\begin{aligned}
&\kappa(F) \triangleq \| F^{-1}\|\cdot\| F\|,\ \Delta\varphi_{l}=\varphi_{l*}-\varphi_{l} \\
&\frac{\|\Delta\varphi_{l}\|}{\|\varphi_{l*}\|}\leq\frac{\| F^{-1}\|\cdot\| F\|}{1-\| F^{-1}\|\cdot\|\Delta F\|}\left(\frac{\|\Delta F\|}{\| F\|}+\frac{\|\Delta\varphi_{m}\|}{\|\varphi_{m}\|}\right) \\
&\xrightarrow{\Delta F\to\mathbf{0}} \frac{\|\Delta\varphi_{l}\|}{\|\varphi_{l*}\|}\leq\kappa(F)\left(\frac{\|\Delta\varphi_{m}\|}{\|\varphi_{m}\|}\right)
\end{aligned}
\tag{10}
$$

For the sake of computational efficiency, we avoid using regularization methods, optimization strategies, and iterative methods with high computational complexity, which are commonly used for large-scale problems. And use a relatively simple and low computational complexity structural dependency method. The calculation of the elements in the inversion coefficient matrix $[F]$ involves only the geometric relationship calculation of the model, the measurement point array, the three-phase conductor and the terrain determine the matrix condition number.

Next, optimize array based on the condition number. Considering operational safety and electrical insulation issues, the maximum height of the array should not exceed the safe distance limit of the transmission line. As shown in Fig.5, set SNR as 40dB. By setting the horizontal distance D_1 between the outer points of the array and the y-axis, and the horizontal distance D_2 between the inner points and the y-axis, set the height h_1 of the outer points and the height h_2 of the inner points of the array. Firstly, calculate the condition number, fix D_2 and h_2, and change D_1 and h_1 as shown in Fig.6 (a); Then fix D_1 and h_1, and change D_2 and h_2 as shown in Fig.6 (b). Then calculate the maximum inversion error, fix D_2 and h_2, and change D_1 and h_1 as shown in Fig.6 (c); Then fix D_1 and h_1, and change D_2 and h_2, as shown in Fig.6 (d).

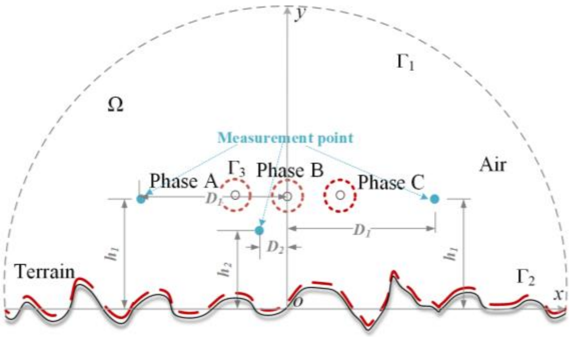

Fig. 5. Geometry of measuring point array.

When D_2 is determined, the influence of D_1 within a certain range on cond(F) is relatively small, but the higher the h_1, the smaller the cond(F). When D_1 is determined, the closer the D_2, the higher the h_2, and the smaller the cond(F). Then analyze the inversion error. D_2 has a greater impact on the error, and the closer the D_2, the smaller the error. For all measurement points, the higher the height, the smaller the error. It is worth pointing out that when the horizontal position is constant, the height reaches a certain value and then increases, and both the condition number and error do not change much. Choosing the highest position outside the safe distance from the field source line can already meet the measurement requirements. Therefore, based on the above principles, the values of the height and spacing of the array measurement points can be obtained when the measurement problem behavior is good. Thus, the optimized array structure was determined.

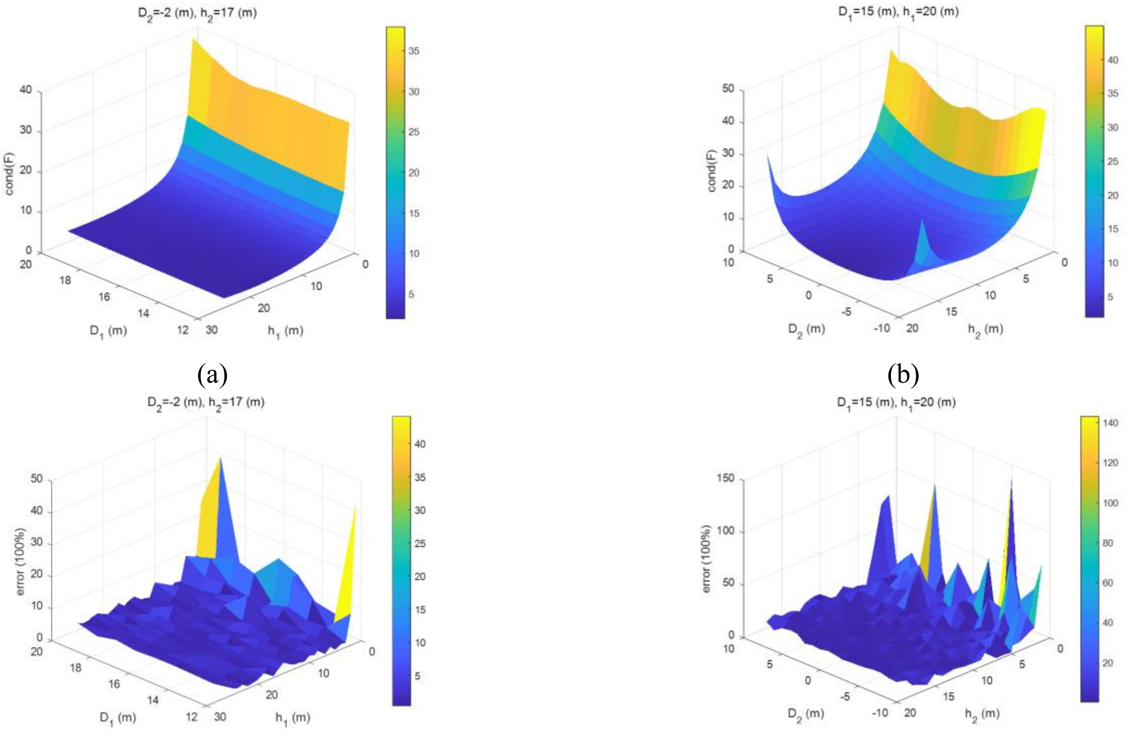

(a) (b)

(c) (d)

Fig. 6. The influence of array on inverse error and condition number (a) outer point position on condition number (b) inner point position on condition number (c) outer point position on inversion error (d) inner point position on inversion error.

3. CASES VALIDATION

In the simulation, we established a 220 kV horizontal single-circuit three-phase transmission line model and set up a potential measurement array consisting of three measurement points in the space below the transmission line. The structural parameters and measurement point parameters are shown in Table 1.

First of all, we employed an analytical case of flat terrain to verify the accuracy of the proposed method, so as to validate the reliability under simple scenarios (general engineering design). Next, in order to further verify the applicability of the model in complex terrains, we introduced a semi-circular terrain analytical case. This terrain simulates the hills or obstacles that may be encountered in reality. Finally, to simulate complex terrains more realistically, we adopted a random terrain generation method to generate 3D terrain models with different roughness levels. These terrain models cover various terrain features ranging from gentle to steep, in order to comprehensively test the applicability of the model.

The parameters transmission line and measurement point locations adopted in this paper comply with the requirements of IEC 61865 [36] regarding the electrical distance. The adopted analysis methods and processes conform to the recommendations in IEEE Std 1597.1-2022 [38] concerning the mathematical level (verification of calculation techniques), implementation level (verification of code implementation through MATLAB), and model level (verification of specific models with COMSOL Multiphysics).

Specifically, we set up analytical cases and 3-D cases, and then compare regional potential, forward calculation time, field source inversion uncertainty and inverse error to verify the effectiveness of the fast forward calculation of spatial potential and robust inversion calculation of field source potential proposed in this paper. The code runs on a laptop with basic hardware parameters of an AMD Ryzen 7 4800U processor integrated with Radeon Graphics core display, a base frequency of 1.80 GHz, and a built-in memory of 16.0 GB. The MATLAB software occupies approximately 3.19 GB of memory when the code runs.

It is worth noting that the uncertainty calculation adopts Type-A standard uncertainty analysis as (11), where V_i is the amplitude for the *i-th* measurement, is the average amplitude of this group measurements, and N is the number of measurements taken in this group. The larger the number of measurements, the smaller the u_A becomes. Considering the limited actual measurements, N is taken as 10, and the results are expressed as per unit value, with the reference value being the field source potential amplitude.

$$u_A(\bar{V}) = \frac{s}{\sqrt{N}},\ s = \sqrt{\frac{1}{N-1}\sum_{i=1}^{N}(V_i - \bar{V})^2} \tag{11}$$

3.1 *Analytical cases*

Firstly, we select two kinds of terrain with analytical solutions for verification, namely flat ground as Fig. 7 (a) and semi-circular terrain as Fig. 7 (b), and directly take a 2-D section here. Both terrains can be solved analytically using the image method. The analytical solution for flat ground is (12), and for semi-circular ground is (13) [36], where p_i represents the coordinates (x, y) at center point of conductor i, the superscript ^{Im} represents the image point, ε is the media permittivity, α_1 is the induction coefficient for flat ground, α_2 is the induction coefficient for semi-circular ground, R_C is the radius of the semi-circular ground, d is the distance from the conductor to the center of the semi-circular ground. For the bundle lines, the conductor radius can be calculated with the equivalent radius R_{eq} as shown in (12), where n_l is the number of conductor splits, r is the radius of sub conductor, and R is the geometric radius of sub conductor arrangement.

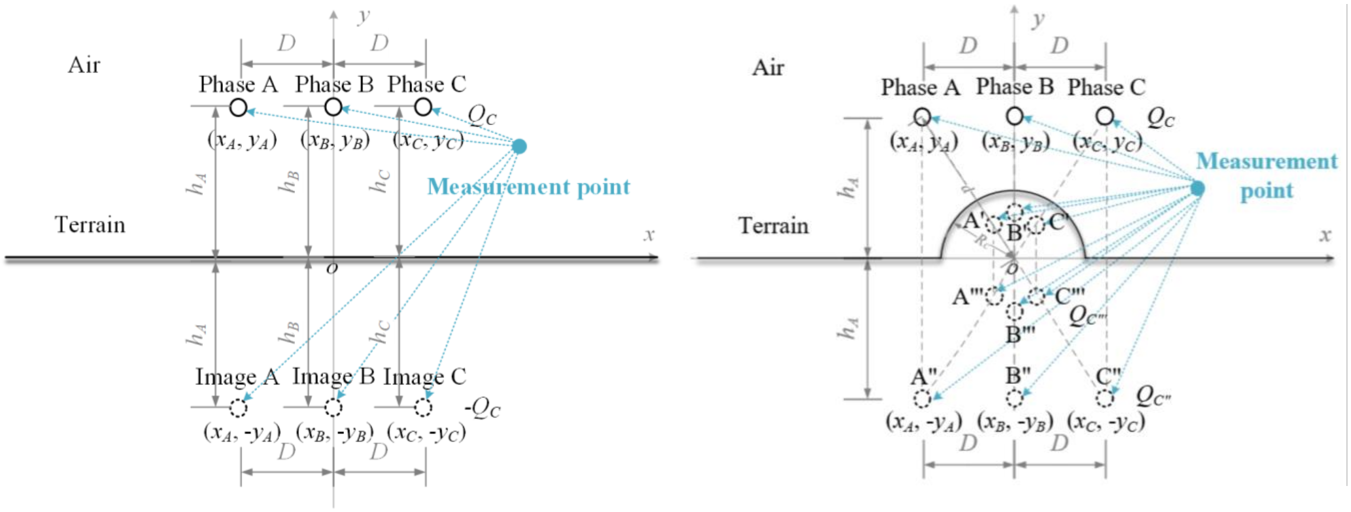

(a) (b)

Fig. 7. Analytical cases solutions using the image method. (a) Case 1: flat terrain. (b) Case 2: semi-circular terrain.

The following is analysis of the calculated results. The method used in this paper adopts all the theories described in Section 2. The original method only uses constant BEM for forward calculation and selects contrast unit for inversion calculation analysis. FEM is also employed for comparative analysis, and the inversion calculations are conducted using the method proposed in this paper. The error analysis will be compared and calculated with the analytical solution of the image method. The calculations after this section all use the same comparative analysis, which will not be mentioned again. To verify the performance of the method, this paper verified the effects of forward calculation and inverse calculation.

TABLE 1
PARAMETERS OF CASES

Parameter	Value
Voltage level	220 kV
Equivalent conductor radius	0.25 m
Conductor diameter	21.6 mm
Conductor spacing	450 mm
Span	150 m
sag	6 m
Lowest suspension height	20.0 m
Phase spacing	11.6 m
Three-phase arrangement	Horizontal
Measurement cross-section	Z=0 m
Measurement unit abscissa	-11.6, 0, 11.6 m
Measurement unit ordinate	18.0 m
Contrast unit abscissa	-21.6, -10, 1.6 m
Contrast unit ordinate	10.0 m
Semi-circle ground radius	4.0 m
Correlation length	4.0 m
RMS Square roughness	1:5
Terms in Karhunen-Loève expansion	80

$$
\begin{gathered}
[\varphi_{l1}] = [\alpha_1(1:3,1:3)][\alpha_1(4:6,4:6)]^{-1}[\varphi_{m1}] \\
\begin{cases}
\alpha_1(i,i) = \dfrac{1}{2\pi\varepsilon}\ln(\dfrac{\left|p_i p_i^{Im}\right|}{R_{eq}}),\ i=j \\
\alpha_1(i,j) = \dfrac{1}{2\pi\varepsilon}\ln(\dfrac{\left|p_i p_j^{Im}\right|}{\left|p_i p_j\right|}),\ i\neq j
\end{cases} \\
R_{eq} = \sqrt[n_l]{r\times n\times R^{n_l-1}}
\end{gathered}
\tag{12}
$$

$$
\begin{gathered}
[\varphi_{l2}] = [\alpha_2(1:3,1:3)][\alpha_2(4:6,4:6)]^{-1}[\varphi_{m2}] \\
\begin{cases}
\alpha_2(i,i) = \dfrac{1}{2\pi\varepsilon}\left(\ln(\dfrac{\left|p_i p_i^{Im}\right|}{R_{eq}}) - \dfrac{R_C}{d}\ln(\dfrac{\left|p_i - kp_i^{Im}\right|}{\left|p_i - kp_i\right|})\right),\ i=j \\
\alpha_2(i,j) = \dfrac{1}{2\pi\varepsilon}\left(\ln(\dfrac{\left|p_i p_j^{Im}\right|}{\left|p_i p_j\right|}) - \dfrac{R_C}{d}\ln(\dfrac{\left|p_i - kp_j^{Im}\right|}{\left|p_i - kp_j\right|})\right),\ i\neq j
\end{cases} \\
d = \left|op_j\right|,\ k = \left(\dfrac{R_C}{d}\right)^2.
\end{gathered}
\tag{13}
$$

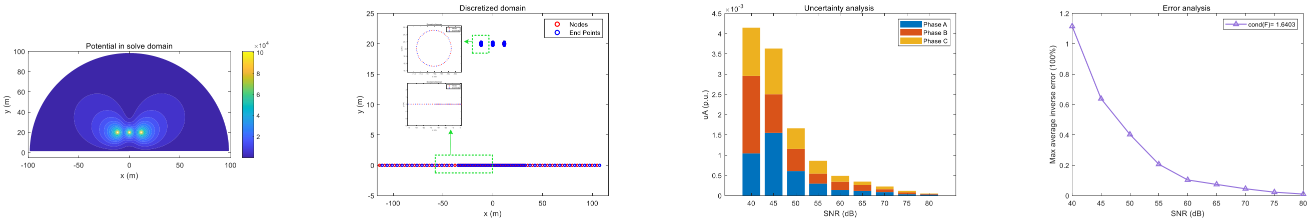

(a1) (b1) (c1) (d1)

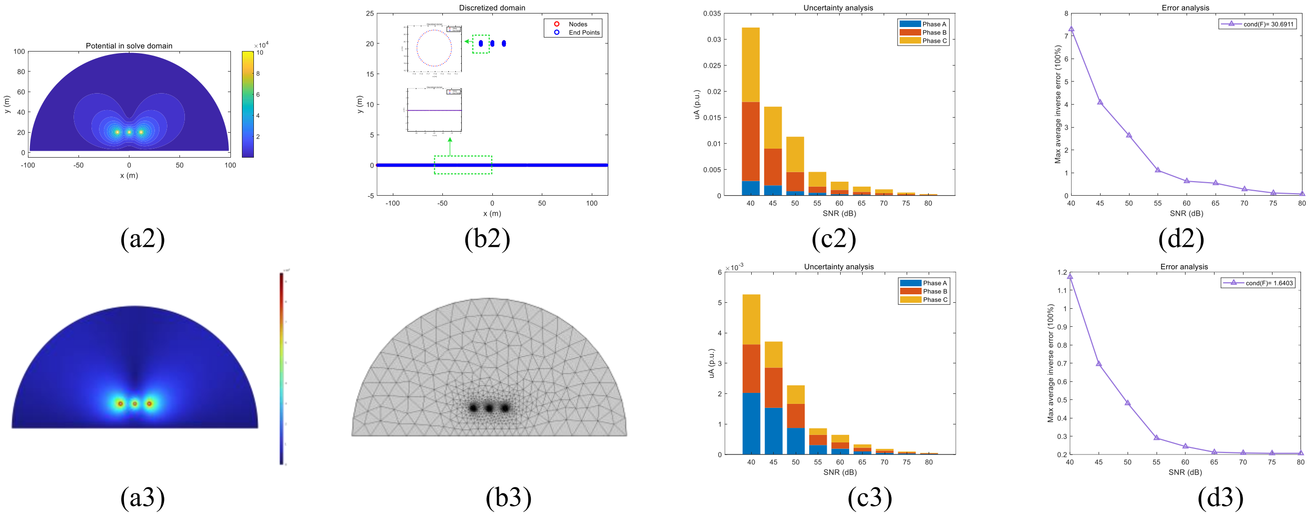

(a2) (b2) (c2) (d2)

(a3) (b3) (c3) (d3)

Fig. 8. Case 1 flat terrain. (a) Forward calculation of potential (b) Forward calculation of discretization elements (c) Inverse uncertainty analysis (d) Inverse error analysis (1) our method (2) original method (3) FEM.

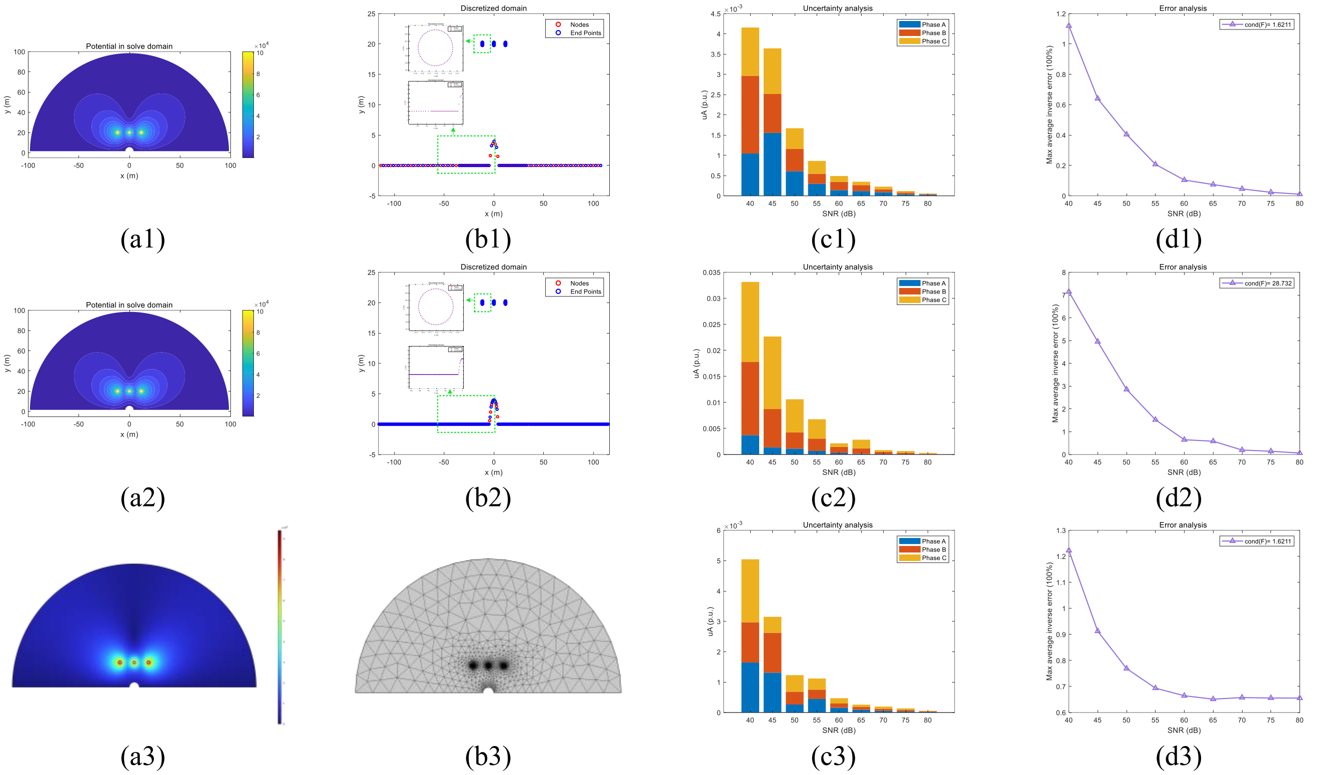

(a1) (b1) (c1) (d1)

(a2) (b2) (c2) (d2)

(a3) (b3) (c3) (d3)

Fig. 9. Case 2 semi-circle terrain. (a) Forward calculation of potential (b) Forward calculation of discretization elements (c) Inverse uncertainty analysis (d) Inverse error analysis (1) our method (2) original method (3) FEM.

1) *Forward calculation of potential distribution*

Firstly, we use both the method proposed in this paper and the original method to calculate the potential distribution, as shown in Fig. 8 (a1) (a2) (a3) and Fig.9 (a1) (a2) (a3), a comparison is made between the measurement point and the analytical solution. As shown in Table 2, in Case 1, the maximum calculation error of our method is 0.15%, while the original method is 0.26% and the FEM is 0.13%. In Case 2, the maximum calculation error of our method is 0.40%, while the original method is 6.70% and the FEM is 0.44%. In Case 1 of ideal flat terrain, all three methods perform well, and the error between our method and FEM is significantly smaller. In Case 2 of semi-circular terrain, the error between the proposed method and FEM is relatively small. However, the error of the original method is relatively large, which is related to the ill-posed characteristics of the coefficient matrix.

2) *Forward calculation time*

Then, we use the unstructured discretization method proposed in this paper and the original method to generate units, as shown in Fig. 8 (b1) (b2) (b3) and Fig.9 (b1) (b2) (b3), the calculation time is compared. As shown in Table 2, in Case 1, the calculation time of our method is 10.52 ms, while the original method is 41.35 ms and the FEM is 1.51 s. In Case 2, the calculation time of this method is 10.38 ms, while the original method is 46.42 ms and the FEM is 1.60 s. Compared with other methods, the speed-up ratio exceeds threefold. Clearly, the computation time of FEM is significantly longer than BEM. This is because FEM requires the internal discretization of the air domain to generate mesh elements, whereas BEM only necessitates discretization on the boundaries. Although BEM generates a dense coefficient matrix, it still offers higher computational efficiency than FEM in this specific problem. The calculation time of our method is much shorter than the original method, and less than 20 ms (50Hz) of one voltage cycle, which can achieve fast forward potential calculation.

3) *Inverse uncertainty analysis*

Next, we use our method and the original method to inverse the source voltage and calculate the Type-A standard uncertainty at different SNR (signal-to-noise ratios). To visually represent the sum of the absolute values of the three-phase uncertainties, the results are presented in a stacked bar chart, as shown in Fig. 8 (c1) (c2) (c3) and Fig.9 (c1) (c2) (c3). The larger the SNR, the smaller the uncertainty. As shown in Table 2, when SNR=40dB and in Case 1, the maximum three-phase uncertainty of our method is 1.91E-3 p.u., while the original method is 1.52E-2 p.u. and the FEM is 2.03E-3 p.u. In Case 2, the maximum uncertainty of the three-phase in this method is 1.92E-3 p.u., while the original method is 1.52E-2 p.u. and the FEM is 2.28E-3 p.u. The uncertainty of the method proposed in this paper is similar to the performance of FEM, and is an order of magnitude lower than the original method.

4) *Inverse error analysis*

Finally, we use the method proposed in this paper and the original method to inverse the field source voltage and compared the maximum three-phase average inversion error under different SNR (signal-to-noise ratio), as shown in Fig.8 (d1) (d2) (d3) and Fig.9 (d1) (d2) (d3). The larger the SNR, the smaller the error. As shown in Table 2, in the case of strong noise with SNR=40dB and flat terrain in Case 1, the maximum average inversion error of our method is 1.12%, while the original method is 7.29% and the FEM is 1.17%. In Case 2, the maximum calculation error of our method is 1.12%, while the original method is 7.15% and the FEM is 1.15%. The calculation error of this method is stable and significantly better than the original method, and is comparable to the error with FEM. Compared to the original method, when using the inversion approach proposed in this paper, the condition number of the transformation matrix is greatly reduced, effectively minimizing inversion errors in noisy environments.

Overall, compared to analytical solutions, our method shows good performance in terms of calculation error at measurement points, forward calculation time, and uncertainties and errors in inversion; to FEM, this method requires less computation time, with minor differences in other aspects; to the original method, there is significant improvement in all four comparative indicators with the method proposed in this paper.

TABLE 2
RESULT ANALYSIS

Case	Contrast	Maximum forward calculation error at the measuring point	Forward calculation time	Maximum uncertainty of three-phase	Maximum average inversion error of three phases
Case 1	Our method	0.15%	10.52 ms	1.91E-3p.u.	1.12%
	Original method	0.26%	41.35 ms	1.52E-2p.u.	7.29%
	FEM	0.13%	1.51 s	2.03E-3p.u.	1.17%
Case 2	Our method	0.40%	10.38 ms	1.92E-3p.u.	1.12%
	Original method	6.70%	46.42 ms	1.54E-2p.u.	7.15%
	FEM	0.44%	1.60 s	2.28E-3p.u.	1.15%

3.2 *3-D cases*

Next, this paper will discuss the adaptability of the proposed method in 3-D scenarios. As our method is based on a simplification to a 2-D cross-section, its adaptability to 3-D models depends on terrain variations in the z-direction. This paper employs Karhunen-Loève Expansion (KLE) [39]-[41] to analyze random terrain. KLE decomposes the random field into a series of orthogonal basis functions through eigenvalue decomposition. The specific terrain generation method, as described in (14), differs from a direct 3-D KLE. Instead, we use two 1-D KLE to generate the random terrain $Y(x, z)$. Initially, a 1-D KLE $Y_{KLE1}(x)$, is performed in the xy-direction, followed by a second 1-D KLE $Y_{KLE2}(z)$, to simulate the terrain undulations in the z-direction.

In this model, the mean function of the random terrain is set to zero, and the covariance function C uses a Gaussian covariance function. The eigenvalues ω and eigenfunctions τ of the covariance function C are computed. ξ represents normally distributed random variables. E_1 and E_2 denote the number of terms in the KLE expansions. S_i and S_j are arbitrary points. L is the Correlation Length, indicating the range of spatial correlation. σ represents the RMS Surface Roughness, controlling the variability of the random field. σ_x corresponds to KLE1, and σ_z to KLE2.

$$
\begin{gathered}
\mathrm{Y}(x,z) = Y_{KLE1}(x) + Y_{KLE2}(z) \\
\begin{cases}
Y_{KLE1}(x) = \sum_{e_1=1}^{E_1} \sqrt{\omega_{e_1}}\,\tau_{e_1}(x)\xi_{e_1} \\
Y_{KLE2}(z) = \sum_{e_2=1}^{E_2} \sqrt{\omega_{e_2}}\,\tau_{e_2}(z)\xi_{e_2} \\
C(S_i,S_j) = \sigma^2 \exp\left(-\dfrac{|S_i - S_j|}{L}\right)
\end{cases}
\end{gathered}
\tag{14}
$$

Analysis of Case 3 and Case 4 is conducted in *1)-4)*, with *5)* corresponding to the analysis when the Root Mean Square (RMS) Surface Roughness σ changes. In Case 3, σ_x=1 and σ_z=0, the discussion is on terrain undulations only in the xy-directions with no change in the z direction, as shown in Fig. 10 (a1). In Case 4, σ_x=1 and σ_z=1, the discussion covers terrain undulations in the xyz-direction, as shown in Fig. 11 (a1). The last subsection *5)* analyzes the performance of the method when RMS Surface Roughness σ ranges from 1 to 5, with results for different σ values presented only due to paper length limitations.

It is worth noting that the measurement points used in the inversion calculations are 3-D simulation results (with noise added), conducted using COMSOL Multiphysics. To control comparison conditions, meshing no longer utilizes the software's fully adaptive division but rather a constrained division with cell size restrictions to ensure that most terrain details are addressed. In the software solution, geometric shape functions are set to quadratic Lagrange elements. Due to the presence of the random variable ξ, the same RMS Surface Roughness σ can generate different random terrains.

The following is analysis of the calculated results, with specific details as follows:

1) Forward calculation of potential distribution

Firstly, we used BEM software to calculate the 3-D model, and the method proposed in this paper to compute the potential distribution, as shown in Fig. 10 (a2) and Fig.11 (a2). As shown in Table 3, in Case 3, the maximum calculation error of our method is 0.15%; In Case 4, the maximum calculation error of our method is 0.32%. The method proposed in this paper can still effectively calculate the forward potential when applied to the 3-D scenario.

2) Forward calculation time

Secondly, we used the unstructured discretization method proposed in this paper and the 3-D model discretization to generate units, as shown in Fig. 10 (b1) (b2) and Fig. 11 (b1) (b2), the calculation time was compared. As shown in Table 3, in Case 3 the calculation time of our method is 10.03 ms, while the 3-D model solution takes 97.76 s. In Case 4, the calculation time of our method is 10.64 ms, while the 3-D model solution takes 139.70 s. Calculation time of our method is much shorter than that of the 3-D model, and less than one voltage cycle, which can achieve fast forward potential calculation.

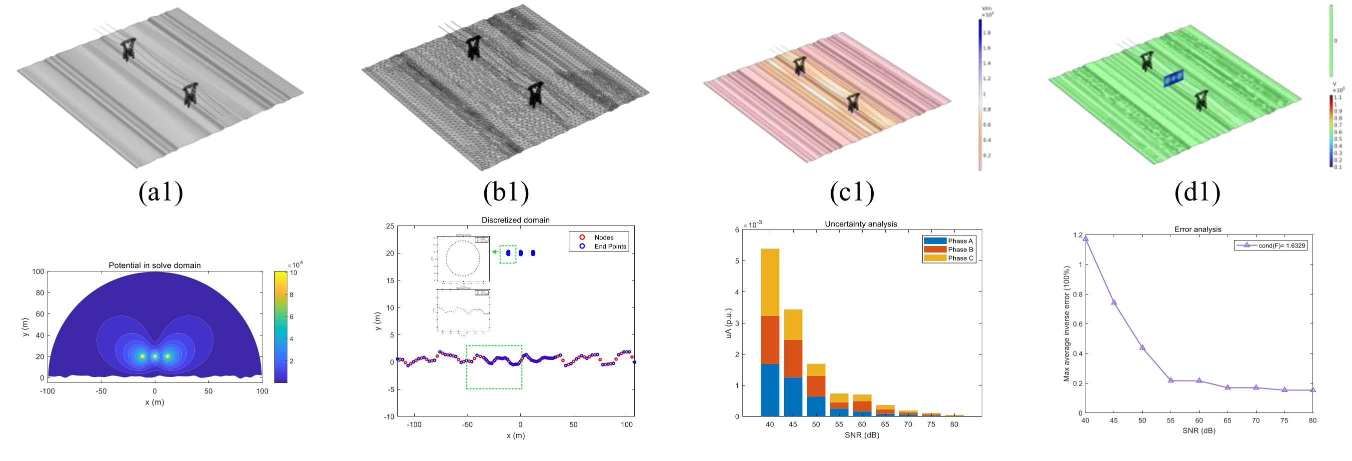

(a1) (b1) (c1) (d1)

(a2) (b2) (c2) (d2)

Fig. 10. Case 3: σ_x=1, σ_z=0. (a1) 3-D model geometry (b1) 3-D model discretization elements (c1) 3-D model electric field (d1) 3-D model potential (a2) Forward calculation of potential (b2) Forward calculation of discretization elements (c2) Inverse uncertainty analysis (d2) Inverse error analysis.

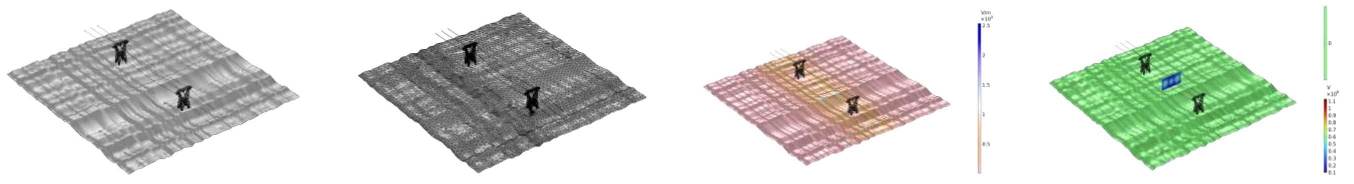

(a1) (b1) (c1) (d1)

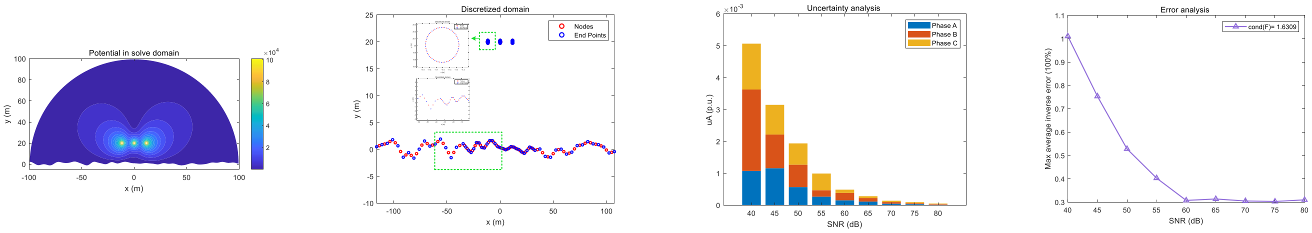

(a2) (b2) (c2) (d2)

Fig. 11. Case 4: σ_x=1, σ_z=1. (a1) 3-D model geometry (b1) 3-D model discretization elements (c1) 3-D model electric field (d1) 3-D model potential (a2) Forward calculation of potential (b2) Forward calculation of discretization elements (c2) Inverse uncertainty analysis (d2) Inverse error analysis.

3) Inverse uncertainty analysis

Then, we used the method proposed in this paper to inverse and calculate the uncertainty of the field source voltage at different SNR. As shown in Fig. 10 (c2) and Fig. 11 (c2), the larger the SNR, the smaller the uncertainty. When SNR=40dB, the method proposed in this paper performs well in both cases, with a maximum three-phase uncertainty of less than 2.55E-3 p.u., indicating the robustness of the inversion calculation in this paper.

4) Inverse error analysis

Next, we added noise to the measurement points of the 3-D simulation model and used our method to inverse the field source voltage. We also compared the maximum three-phase average inversion error at different SNR. As shown in Fig. 10 (d2) and Fig. 11 (d2), the larger the SNR, the smaller the error. As shown in Table 3, in Case 3 of strong noise with SNR=40dB, the maximum average inversion error of our method is 1.35%. In Case 4, the maximum calculation error of the method proposed in this paper is 1.01%, further demonstrating the effectiveness of the inverse calculation of electric potential in this paper.

TABLE 3

RESULT ANALYSIS

Case	Contrast	Maximum forward calculation error at the measuring point	Forward calculation time	Maximum uncertainty of three-phase	Maximum average inversion error of three phases
Case 3	Our method	0.15%	10.03 ms	2.52E-3p.u.	1.35%
	3-D method	—	97.76 s	—	—
Case 4	Our method	0.32%	10.64 ms	2.55E-3p.u.	1.01%
	3-D method	—	139.70 s	—	—

5) RMS Surface Roughness analysis

Finally, we vary the σ to compute the forward calculation time and the maximum error at the measurement points; when the SNR=40dB, we calculate the maximum inversion error and the maximum uncertainty. The cases are divided into two kinds: $\sigma_x \neq 0$, $\sigma_z=0$ and $\sigma_z \neq 0$, $\sigma_x=1$. The condition $\sigma_x \neq 0$, $\sigma_z=0$ indicates no terrain variation in the z-direction, clearly the 2-D simplified model used in this paper is based on this assumption. Meanwhile, to discuss the adaptability and limitations of this method when there is terrain variation in the z-direction, $\sigma_z \neq 0$, $\sigma_x=1$ corresponds to cases with terrain variation in the z-direction. $\sigma \neq 0$ corresponds to σ spaced at intervals of 1-5, used to discuss the performance of this method when the degree of terrain variation varies. Two points are worth noting: first, even in cases where there is terrain variation in the z-direction, this method still retains some adaptability because measurement points are chosen closer to the source and away from the terrain to ensure robustness of the inversion; secondly, σ does not correspond to the maximum terrain deviation, for instance, a randomly generated terrain with σ_z=5, σ_x=1 might have a maximum elevation of 6.89 m, and related conclusions are only applicable to the corresponding model.

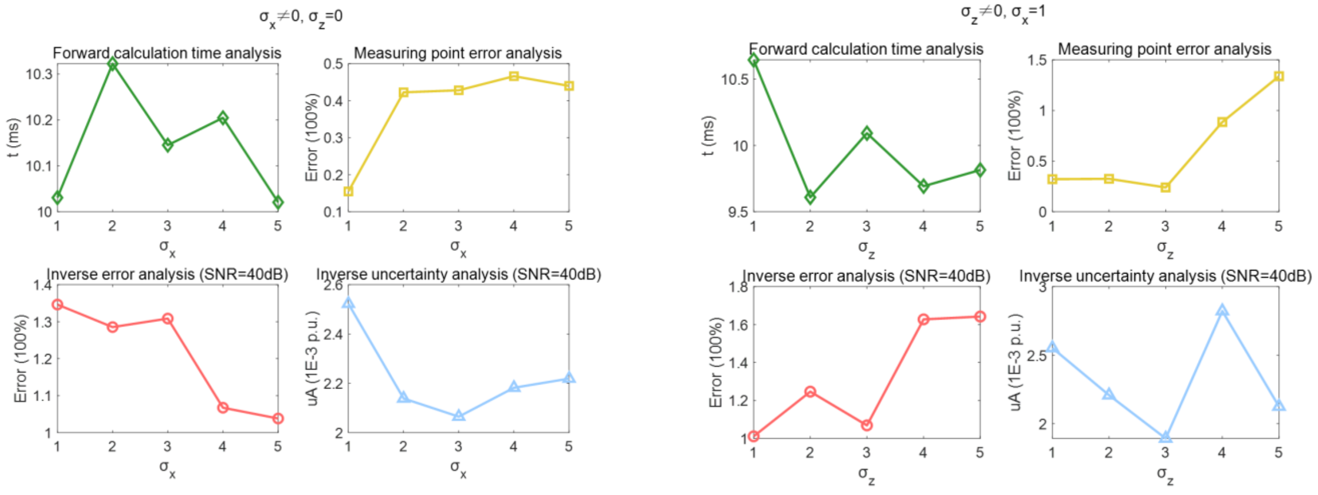

(a) (b)

Fig. 12. RMS Surface Roughness analysis (a) $\sigma_x \neq 0$, $\sigma_z=0$ (b) $\sigma_z \neq 0$, $\sigma_x=1$.

When $\sigma_x \neq 0$ and $\sigma_z=0$, there is no terrain variation in the z-direction. As shown in Fig.12 (a), for forward calculation, the maximum computation time is 10.32 ms, and the maximum error at the measurement points is 0.47%. As σ_x increases, fluctuations in computation time and maximum error at the measurement points are relatively small. For inversion calculations under noise environment (SNR=40dB), the maximum inversion error from the source is 1.35%, and the maximum uncertainty in the inversion is 2.52E-3 p.u. As σ_x increases, the inversion error and maximum uncertainty remain relatively stable.

When $\sigma_z \neq 0$ and $\sigma_x=1$, there is terrain variation in the z-direction. As shown in Fig.12 (b), for forward calculation, the maximum computation time is 10.64 ms, and the maximum error at the measurement points is 1.34%. As σ_z increases, fluctuations in computation time are relatively small; however, the maximum error at the measurement points increases, remaining below 1% when σ_z is less than 5. For inversion calculations in a noisy environment (SNR=40dB), the maximum inversion error from the source is 1.64%, and the maximum uncertainty in the inversion is 2.82E-3 p.u. As σ_z increases, the inversion error also increases, remaining below 1.5% when σ_z is less than 4; the maximum uncertainty in the inversion remains relatively stable.

The results above indicate that the method proposed in this paper maintains accuracy within a certain range of surface roughness in the z-direction, and demonstrates a degree of adaptability to three-dimensional scenarios, primarily depending on the error tolerance requirements. However, it is important to note that in high-precision applications, more detailed three-dimensional analysis is still required, particularly in cases where computational resources are abundant and real-time feedback is not necessary. On the other hand, in real-time or large-scale monitoring applications, since it is not necessary to place measurement points at every span, a preliminary assessment of terrain roughness can be conducted to select appropriate monitoring areas, followed by simplified analysis of selected cross-sections. Future research could further explore hybrid modeling strategies that combine 2D simplifications with localized 3D refinements, to enhance the method's adaptability to more complex terrain conditions.

4. CONCLUSION

This paper proposes a numerical model for fast calculation of spatial potential and robust inversion of field source voltage of overhead transmission lines under complex terrain conditions and proves the effectiveness of the method through 2-D analytical and 3-D examples. A basic model based on cross-section is proposed, and the constant BEM is used for solving. An unstructured discretization method is proposed around the measurement array structure, and a robust inversion method for field source voltage based on optimization of the measurement array is presented.

In cases validation, a model of a 220 kV single-circuit overhead transmission line is established. Through analytical examples on flat and semi-circular terrain conditions, it can be seen that compared with traditional method, the maximum calculation error of the model proposed in this paper is less than 0.5%, and the total calculation time is less than 15 ms; In a strong noise environment (SNR=40dB), the uncertainty and maximum error of the inversion calculation are reduced by one order of magnitude. The maximum three-phase uncertainty of the inversion is less than 3E-3 p.u., and the maximum three-phase error of the inversion is less than 1.2%.

In the validation of 3-D cases, this paper uses KLE to simulate random terrain, analyzing two types of cases: those without and with changes in terrain along the line direction, using RMS Surface Roughness as the characteristic indicator. The cross-sectional simplification method presented has good adaptability in cases where there is no change in terrain along the line, with small fluctuations in calculation time, maximum error at measurement points, inversion error, and maximum uncertainty in inversion, and parameters similar to those in 2-D cases. In cases with changes in terrain along the line, when the RMS Surface Roughness along the line is less than 4, fluctuations in calculation time and maximum uncertainty in inversion are small, with calculation times under 15 ms, inversion uncertainty less than 3E-3 p.u., maximum error at measurement points under 1%, and inversion errors under 1.5%.

This method can achieve fast calculation of spatial potential and robust inversion of field source voltage of transmission lines under complex terrain conditions. The method proposed in this paper is based on a 2-D simplified model, it still exhibits adaptability in 3-D scenarios. In applicable situations, the forward calculation time is less than one voltage cycle (50Hz), the inversion uncertainty is less than 3E-3 p.u., and the inversion error is less than 1.5%. It can be applied to online monitoring, state evaluation, and other measurement and evaluation links that require real-time feedback, providing data support and decision-making basis for power system power quality evaluation and operation protection.

CRediT authorship contribution statement

Yuqing Ji: Methodology, Software, Writing. Jiaxin Yuan: Comments, Funding. Igor S. Stievano: Comments, Conception. Riccardo Trinchero: Comments, Conception. Hang Zhou: Comments, Writing.

Declaration of competing interest

The authors declare that they have no known competing financial interests or personal relationships that could have appeared to influence the work reported in this paper.

Acknowledgement

This work was supported in part by the National Natural Science Foundation of China under Grant 52207182 and U2166207, in part by the China Postdoctoral Science Foundation under Grant 2023M732690 and 2024T170677. (Corresponding author: Jiaxin Yuan and Igor S. Stievano.)

Corresponding author

Jiaxin Yuan. E-mail address: yjx98571@163.com. Igor S. Stievano. E-mail address: igor.stievano@polito.it.

REFERENCES

[1] Sendaula, M., Hilson, D. W., Myers, R. C., Akens, L. G., & Woolery, B. J. (1984). Analysis of electric and magnetic fields measured near TVA'S 500-kV transmission lines. *IEEE transactions on power apparatus and systems*, (2), 328-336.

[2] Ahmad, J., Malik, A. S., Xia, L., & Ashikin, N. (2013). Vegetation encroachment monitoring for transmission lines right-of-ways: A survey. *Electric Power Systems Research*, 95, 339-352.

[3] Talaat, M. (2014). Calculation of electrostatically induced field in humans subjected to high voltage transmission lines. *Electric power systems research*, 108, 124-133.

[4] Alhassan, A. B., Zhang, X., Shen, H., & Xu, H. (2020). Power transmission line inspection robots: A review, trends and challenges for future research. *International Journal of Electrical Power & Energy Systems*, 118, 105862.

[5] Almeida, F. S., Silveira, F. H., & Visacro, S. (2024). An expeditious calculation approach to consider the influence of power frequency voltage on the calculation of the lightning performance of transmission lines: Validation for different peak current-front time correlation expressions and cumulative peak current distributions. *Electric Power Systems Research*, 237, 110965.

[6] Ma, Z., Jasni, J., Ab Kadir, M. Z. A., & Azis, N. (2024). Numerical model of lightning attachment on UHV-AC transmission lines and effects of operating voltage, phase angle, and terrain. *Electric Power Systems Research*, 227, 109986.

[7] Diamantis, A., & Kladas, A. G. (2019). Mixed numerical methodology for evaluation of low-frequency electric and magnetic fields near power facilities. *IEEE Transactions on Magnetics*, 55(6), 1-4.

[8] Christopoulos, C. (2022). The transmission-line modeling (TLM) method in electromagnetics. *Springer Nature.*

[9] Zhao, G., Hu, J., He, J., & Wang, S. X. (2020). A novel current reconstruction method based on elastic net regularization. *IEEE Transactions on Instrumentation and Measurement*, 69(10), 7484-7493.

[10] Singer, H., Steinbigler, H., & Weiss, P. (1974). A charge simulation method for the calculation of high voltage fields. *IEEE Transactions on Power Apparatus and Systems*, (5), 1660-1668.

[11] CIGRÉ, G. (1980). Electric and magnetic fields produced by transmission systems.

[12] Sendaula, H. M., Johnson, R. R., Hilson, D. W., & Meyer, R. C. (1983). Electric fields induced by EHV transmission over irregular terrain. *IEEE Transactions on Power Apparatus and Systems*, (5), 1452-1458.

[13] Zhou, H. W. (2017). Measurement of Electromagnetic Parameters of Trees and Their Impact on the Electric Field of Transmission Lines. *Harbin: Northeast Forestry University*.

[14] El Dein, A. Z. (2009). Magnetic-field calculation under EHV transmission lines for more realistic cases. *IEEE Transactions on Power Delivery*, 24(4), 2214-2222.

[15] Trlep, M., Hamler, A., Jesenik, M., & Stumberger, B. (2009). Electric field distribution under transmission lines dependent on ground surface. *IEEE Transactions on Magnetics*, 45(3), 1748-1751.

[16] Farah, A. A., Afonso, M. M., Vasconcelos, J. A., & Schroeder, M. A. (2017). A finite-element approach for electric field computation at the surface of overhead transmission line conductors. *IEEE Transactions on Magnetics*, 54(3), 1-4.

[17] Diamantis, A., & Kladas, A. G. (2019). Mixed numerical methodology for evaluation of low-frequency electric and magnetic fields near power facilities. *IEEE Transactions on Magnetics*, 55(6), 1-4.

[18] Liu, Y. J., & Nishimura, N. (2006). The fast multipole boundary element method for potential problems: a tutorial. *Engineering Analysis with Boundary Elements*, 30(5), 371-381.

[19] Lee, J., Kim, J. H., Chung, Y. S., & Jung, H. K. (2020). Analysis of Electric Field for Overhead Power Transmission Lines by Using 3-D Method of Moment. *Journal of Electrical Engineering & Technology*, 15, 1313-1322.

[20] Zheng, Z. Y., Su, Z., Lu, F., Jin, Y., Liu, T., & Zou, J. (2020). Nominal field calculation of HVDC transmission lines over an irregular terrain by using fast adaptive BEM. *High Voltage Apparatus*, 56(2), 34-39.

[21] Li, R. F., Du, H., Li, K. Q., Wang, J., Gao, C. X., & Cao, X. B. (2021). Study on space electric field calculation method of 3D terrain. *High Voltage Apparatus*, 57(4), 47-54.

[22] Leman, J. T., & Olsen, R. G. (2021). Fourier enhanced charge simulation method for electrostatic analysis of overhead transmission lines. *IEEE Transactions on Power Delivery*, 37(2), 1078-1087.

[23] Lelievre, P. G., & Farquharson, C. G. (2013). Gradient and smoothness regularization operators for geophysical inversion on unstructured meshes. *Geophysical Journal International*, 195(1), 330-341.

[24] Zhu, K., Lee, W.-K., & Pong, P. W.-T. (2019). Non-contact voltage monitoring of HVDC transmission lines based on electromagnetic fields. *IEEE Sensors Journal*, 19(8), 3121–3129.

[25] Chen, K.-L., & Chen, H.-S. (2024). Implementation and feasibility of environmental electric field measurement based on unmanned aerial vehicle. *IEEE Transactions on Power Delivery*, 39(3), 1877–1888.

[26] Sun, X., Huang, Q., Jiang, L. J., & Pong, P. W. T. (2013). Overhead high-voltage transmission-line current monitoring by magnetoresistive sensors and current source reconstruction at transmission tower. *IEEE transactions on magnetics*, 50(1), 1-5.

[27] Wu, Y., Zhao, G., Hu, J., Ouyang, Y., Wang, S. X., He, J., ... & Wang, S. (2019). Overhead transmission line parameter reconstruction for UAV inspection based on tunneling magnetoresistive sensors and inverse models. *IEEE Transactions on Power Delivery*, 34(3), 819-827.

[28] Mukherjee, M., Olsen, R. G., & Li, Z. (2020). Noncontact monitoring of overhead transmission lines using space potential phasor measurements. *IEEE Transactions on Instrumentation and Measurement*, 69(10), 7494-7504.

[29] Qi, Y., Li, X., Yin, C., Li, H., Qi, Z., Zhou, J., ... & Ren, X. (2020). 3-D time-domain airborne EM inversion for a topographic earth. *IEEE Transactions on Geoscience and Remote Sensing*, 60, 1-13.

[30] Liu, J., Ren, Z., Xiao, X., Tang, J., & Lin, P. (2022). Accelerating the frequency domain controlled-source electromagnetic data inversion using rational Krylov subspace algorithm. *IEEE Transactions on Geoscience and Remote Sensing*, 60, 1-12.

[31] Xing, Y., Liu, J., Li, F., Zhang, G., & Li, J. (2024). Non-Contact Voltage Reconstruction Method Based on Dual-Pin Type Probes Structure and Measuring Point Optimization for AC Overhead Transmission Lines. *IEEE Transactions on Instrumentation and Measurement*.

[32] Mai, Y., Xing, Y., Ye, Z., Zhang, G., & Li, J. (2024). Current Reconstruction and Sag/Wind Deflection Monitoring of Transmission Lines by Magnetic Sensing. *IEEE Transactions on Instrumentation and Measurement*.

[33] Chen, K. (2005). Matrix preconditioning techniques and applications (No. 19). *Cambridge University Press*.

[34] Xu, W., Huang, Z., Xie, X., & Li, C. (2021). Synchronized waveforms–a frontier of data-based power system and apparatus monitoring, protection, and control. *IEEE Transactions on Power Delivery*, 37(1), 3-17.

[35] Gautschi, W. (2011). Numerical analysis. *Springer Science & Business Media*.

[36] Lacava, F. (2016). *Classical electrodynamics: From image charges to the photon mass and magnetic monopoles* (2nd ed.). Springer International Publishing. (pp. 35-52)

[37] International Electrotechnical Commission. (2001). Overhead lines - Calculation of the electrical component of distance between live parts and obstacles - Method of calculation (IEC 61865:2001).

[38] IEEE Standards Association. (2022). IEEE standard for validation of computational electromagnetics computer modeling and simulations. In IEEE Std 1597.1-2022 (Revision of IEEE Std 1597.1-2008), 1-52.

[39] Wang, C., Li, Y., Li, Y., Fan, Y., & Feng, Z. (2024). Coupling effect of large deformation and surface roughness on dynamic frictional contact behaviors of hyperelastic material. *Computational Mechanics*, 1-19.

[40] Gladwin, K. T. J., & Vinoy, K. J. (2022). Modeling of spatial permittivity variations using Karhunen–Loève expansion for stochastic electromagnetic problems. *International Journal of RF and Microwave Computer-Aided Engineering*, 32(9), e23250.

[41] Siripatana, A., Le Maitre, O., Knio, O., Dawson, C., & Hoteit, I. (2020). Bayesian inference of spatially varying Manning'sn coefficients in an idealized coastal ocean model using a generalized Karhunen-Loève expansion and polynomial chaos. *Ocean Dynamics*, 70, 1103-1127.